STUDIES ON PREPARATION TECHNICS AND PROPERTIES OF NANOMATERIALS FOR MEDICAL APPLICATIONS

Ph.D. Thesis

Szabolcs Beke, M.Sc.

Supervisors: Dr.habil. József Géza Kiss, Prof. Dr. Viatcheslav Safarov
Program leader: Prof. Dr. Gábor Jancsó

Department of Otolaringology, Faculty of Medicine,
University of Szeged, Hungary
&
CRMCN-CNRS, Faculté de Science de Luminy,
Université de la Mediterranée, Marseille, France

2007

PAPERS RELATED TO THE THESIS:

I. Manufacturing of porous silicon; Porosity and thickness dependence on electrolyte composition, Applied Surface Science 178, 190-193, 2001
K.Kordás, J. Remes, **S. Beke**, T.Hu, S. Leppavuori

II. Sructural and optical properties of pulsed laser deposited V_2O_5 thin films (to be published in Thin Solid Films)
S. Beke, S. Giorgio, L. Kőrösi, L. Nánai, W. Marine

III. Nd:YAG laser synthesis of nanostructural V_2O_5 from vanadium oxide sols; morphological and structural characterizations (to be published in Applied Surface Science)
S. Beke, L. Kőrösi, S. Papp, L. Nánai, A.Oszkó, J. G. Kiss, V. Safarov

PAPERS NOT RELATED TO THE THESIS:

IV. Optical properties of porous silicon Part I, Fabrication and investigation of single layers, Optical Materials 25(3):251-255, 2004
K.Kordás, A.E.Pap, **S. Beke,** S. Leppavuori

V. Optical properties of porous silicon Part II, Fabrication and investigation of multilayer structures, Optical Materials 25(3): 257-260, 2004
K.Kordás, **S. Beke**, A.E.Pap, A. Uusimaki, S. Leppavuori

ACKNOWLEDGMENTS

This study has been accomplished in the frame of a bilateral program between France and Hungary. One part of the work was carried out in CRMC-N in Marseille, France. The other part was accomplished in Hungary at the laboratories of the University of Szeged during the years of 2002-2006. Straightforwardly, the work was financially supported by both the French and the Hungarian governement. Thus, I am very grateful to Prof. Dr. Viatcheslav Safarov and Dr. Wladimir Marine for giving me the possibility to work in the laboratories of CRMC-N in Marseille, France.

I wish to thank to my supervisor, Dr. habil. József Géza Kiss for giving me the opportunity to work as a PhD student in his group at the Department of Otolaryngology, Faculty of Medicine, University of Szeged.

I would like to express my gratitude to Prof. Dr. László Nánai, the tutor of my studies, for his continous support, help and patience during my studies and research work.

I also want to acknowledge László Kőrösi, Dr. Szilvia Papp, Prof. Dr. Imre Dékány of the Department of Colloids and Dr. Suzanne Giorgio of CRMCN for the continous cooperation and useful discussions.

Szeged, August 2007

Szabolcs Beke

LIST OF SYMBOLS AND ABBREVIATIONS

FESEM	Field-emission electron microscopy
FWHM	Full width at half maximum
HRTEM	High resolution transmission electron microscopy
NC	Nanocluster
Nd:YAG	Neodimium: Yttrium Aluminium Iron Garnet
PLA	Pulsed laser ablation
PLD	Pulsed laser deposition
PS	Porous silicon
SEM	Scanning electron microscopy
TEM	Transmission electron microscopy
XRD	X-ray diffraction
XPS	X-ray photoelectron spectroscopy

CONTENTS

1. INTRODUCTION

Nanotechnology and nanoscience have been developing very fast in the past few years. Many materials and devices created in the nanoscale range show new and improved properties and functionalities compared to the bulk materials.

This thesis is about science on a nanoscale range - an interdisciplinary approach to nanoparticles. Studies of the preparation technics of nanoparticles using both physical and chemical methods are presented.

Understanding and controlling factors for particle growth during synthesis are the keys for successful fabrication of materials with tailored properties. The size effects on optical properties have been examined. The relationship between the experimental parameters and the film properties / nanocluster (NC) dimensions has been investigated in several cases.

Much of the excitement surrounding nanochemistry resides in the promise that materials fabricated in this size range may exhibit unique structural properties and chemical reactivity. It is evident that the reduced size of nanoparticles yields a more efficient catalysis due to the fact that the surface-to-volume ratio is increased. Besides, the size decrement of the material goes together with a change of physical properties, which opens another field for the exploitation of nanoclusters (NCs). However, when the material is sampled in a sufficiently small amount - typically 10 nanometers or less - the physical properties change due to quantum confinement that results from electrons and holes being squeezed into a dimension that approaches a critical quantum measurement, called the exciton Bohr radius.

In chapter 3., we show the process of porous silicon (PS) manufacturing by electrochemical etching. PS - unlike bulk Si – is *biocompatible*. As this material has a huge surface and exhibits a high degree of biocompatibility, it can be very useful for biomedical applications. The large surface area enables bio-organic molecules to adhere well. It degrades silicic acid, which causes no harm to the body. This has opened potential applications in medicine such as a framework of the growth of bone.

In chapter 4., we present nanocrystalline vanadium oxide thin films elaborated by means of pulsed laser deposition that is a great tool in NC synthesis. We discuss the experimental set up in details. The energy of laser light absorbed by target material is converted to the kinetic energy of atoms leaving target surface. Under conditions of laser ablation, the removal of particles is massive and they form a hot and dense plasma. The density and pressure gradients lead to the expansion of plasma cloud directed from the target surface. During the expansion, laser-induced plasma plume cools down adiabatically. When the temperature becomes low enough for condensation of vapor, the NCs are formed. The presence of a moderate and controlled ambient atmosphere strongly modifies the hydrodynamics of plasma expansion favoring NC synthesis by the plume confinement effect. The NCs formed in the gas phase are consequently collected onto a substrate forming a nanostructured film. We present the basic mechanisms of synthesis of NCs by pulsed laser ablation and their deposition in form of thin films.

The chapter 5. presents the work on vanadium oxide thin films prepared by sol-gel method, then subjected to Nd:YAG laser (CW, 1064 nm) radiation. The characteristics of the films were changed by varying the intensity of the laser radiation.

During our work, the nanocrystalline films were characterized by XRD, TEM, SEM and XPS for structural, morphological, and chemical analysis.

For the simplicity, references are always found right after the corresponding chapter.

2. CHARACTERIZATION METHODS

2.1. X-ray diffraction

The structural characterizations of the films were studied by XRD using a Philips PW 1830 powder diffractometer using Ni-filtered Cu-K_α radiation (0.15406 nm). The mean crystallite size (D) was calculated from the full width at half maximum (FWHM) of the corresponding X-ray diffraction peaks using Scherrer's formula $D = K\lambda/(\beta\cos\theta)$, where K=0.9 (K is a constant depending on the particle shape), λ is the wavelength of the X-ray radiation, β is the FWHM and θ is the angle of reflection.

2.2. X-ray photoelectron spectroscopy

The surface chemistry study of the samples was performed using the XPS technique. The surface composition and contamination were studied at room temperature. The pressure in the analysis chamber was about 3.0×10^{-9} Torr.

XP spectra were taken with a SPECS instrument equipped with a PHOIBOS 150 MCD 9 hemispherical electron energy analyzer operated in the FAT mode. The excitation source was the non-monochromatic K_α radiation of a magnesium anode (hν = 1253.6 eV). The X-ray gun was operated at 210 W (14 kV, 15mA). The incident angle of the X-ray beam was 45° with respect to the surface normal. The pass energy was set to 20 eV, the step size was 25 meV, and the collection time in one channel was 100 ms. Typically five scans were added to get a single spectrum. The C 1s binding energy of adventitious carbon was used as energy reference: it was taken 285.1 eV. For data acquisition and evaluation both manufacturer's (SpecsLab2) and commercial (CasaXPS, Origin) software were used.

2.3. Optical transmission

Optical transmission measurements were taken by StellarNet EPP2000 spectrometer with a wavelength resolution of ± 0.75 nm

2.4. Transmission and scanning electron microscopy

Transmission electron microscopy (TEM) is an excellent tool to study the particle size, morphology and crystal structure. Samples do not need to be conductive unlike in SEM and STM. TEM gives a good resolution down to a nanometer scale. In TEM there is the possibility of obtaining electron diffraction patterns to identify the crystal structure as well as to use EDX to study the local chemical composition of the samples. In this work, a JEOL 3010 electron microscope working at 300 kV was used. Small pieces of the surface were collected by the microcleavage technique.

In case of sol-gel samples we used Philips CM-10 transmission electron microscope with an accelerating voltage of 100 kV. The microscope was equipped with a Megaview II digital camera. Aliquots of the aqueous dispersion of the samples were dropped on copper grids (diameter 2 mm) covered with Formwar foil, which were transferred into the microscope after drying.

Scanning electron microscopy was performed using a Hitachi S-4700 electron microscope.

3. MANUFACTURING OF POROUS SILICON

3.1. Outline history of porous silicon

Porous silicon (PS) is not a new material, but it is only recently that its true microstructure and surprising properties have come under close investigations. The Uhlirs at Bell Labs in the USA made first PS some 45 years ago [1]. During studies of electropolishing of Si in hydrogen-fluoride based solutions they observed that the surfaces often developed a matte black, brown or red deposit. The deposits were tentatively supposed to be a Si suboxid and for the next decade largely remained an unwanted scientific curiosity. One year after the original work, Fuller and Ditzenberger reported that similar films could develop in HF-HNO3 solutions without any externally applied electrical bias to the Si. The anodized films first received more detailed study by Turner and the chemical stain films by Archer. These films were not recognised as being PS. It was Watanabe and co-workers who first reported their porous nature and the ease with which the material could be inverted into thick Si oxide films.

Before 1990 there were hardly any papers published dealing with PS. There were less than 200 articles, spanning a period of 35 years. In 1991, Lehman and Gösele [6], independently, reported that PS could exhibit an increased band gap compared with bulk silicon and that this property, as well as the formation mechanism itself, involved quantum size effects. Within a year not only multicolour (red-green) photoluminescence, but also forms of visible electroluminescence were achieved, generating considerable excitement. Visible photoluminescence was reported some 16 years ago. The work aroused only minor attention since measurements were restricted to cryogenic temperatures (4,2 K). It was not realised that the radiative processes could occur efficiently at room temperature as well. The origin of the luminescence quickly became a very controversial topic and great numbers of models emerged, each supported by specific observations of the microstructure of the material and the spectroscopic nature of the light emission process.

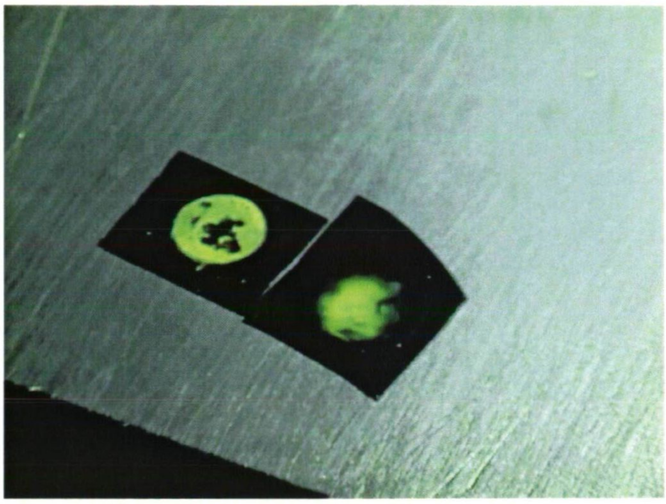

Fig.1. Luminescence was observed for porous layers at yellow-green wavelength. The picture shows true luminescence under UV illumination.

3.2. Current interest in PS

The scientific field of low-dimensional semiconductor structures is a fascinating area of materials science and the one that has a significant technological application. The current world-wide interest in PS resulted primarily from the proposal in 1990 that efficient visible light emission from high porosity structures arises from quantum confinement effects. This is particularly intriguing for two reasons. First, because PS is a silicon structure and Si is spectacularly inefficient at emitting light, even at cryogenic temperatures. Second, because Si is the most technologically important material known to mankind, dominating the microelectronic revolution that influences our everyday lives. Light emitting Si devices could eventually result in a new generation of Si chips and extend the functionality of Si technology from microelectronics into optoelectronics. Moreover, it has efficient biological applications as PS is a biocompatible material and has a huge surface area enabling to connect the microelectronics to biology.

3.3. Structural properties of PS

3.3.1. As-anodised PS

As it is discussed later, the overall structure of PS layers depends very strongly upon anodisation conditions and the resistivity (magnitude and type) of the Si itself. Pore diameters and spacings can vary over a very wide range.

3.3.2. Oxidized PS

Although as-anodised, luminescent PS is hydrogen passivated and contains essentially no oxygen, exposure to ambient air results in progressive modification of the hydrid surface and oxidation of the porous matrix. Furthermore, heating of the PS to high temperature in a strongly oxidising ambient (for example pure oxygen) leads to very fast oxidation of the structure. However, this really oxidized material can still exhibit efficient photoluminescence. This behavior gives important insight of the physical characteristics of the material.

There is a method during PS is deliberately oxidised at high temperature. It is carried out by using of rapid thermal oxidation (RTO), involving transient heating in an oxygen ambient so that careful control of the potentially rapid surface can be maintained.

3.4. Porosity

The term "porous" layer refers to different types of materials that are obtained by electrochemical etching. The characteristics of the so-formed material is very dependant on the type and resistivity of the original substrate and on the electrochemical parameters used during the anodisation process. Therefore, the value of porosity is a macroscopic parameter which does not serve any information about the microstructure of the layer. A much better knowledge of the porous layer is obtained if the pore sizes and their distribution in the material can be determined. To obtain these information are not so easy and different methods have to be used.

The porosity is defined as the fraction of void within the PS layer and can be determined by weight measurements. Three weight measurements are required to get the porosity and the thickness of the layer. The original wafer (m1) is measured before anodisation, then just after anodisation (m2). Finally after dissolution of the whole porous layer in a molar NaOH aqueous solution (m3). Uniform and rapid stripping in the NaOH solution can be obtained if the porous layer is covered with a small amount of ethanol. It improves the infiltration of aqueous NaOH in the pores. After having done these measurements, porosity can easily be calculated by the following equation:

$$P(\%) = (m1\text{-}m2) / (m1\text{-}m3)$$

In case of PS, there has not been any comprehensive study of the pore size distribution so far. The reason is because there are great numbers of parameters which influence this characteristic. All the properties of PS layer, such as the above mentioned porosity, pore diameter, microstructure are strongly dependent on the anodisation conditions. These conditions include HF concentration, pH of the solution and its chemical composition, wafer type and resistivity, current density, crystallographic orientation, temperature, anodisation (etching) time, stirring conditions and illumination during anodisation. Optimum control of the fabrication and reproducibility are only possible if each parameter listed above are taken into account.

3.4.1. Determination of pore sizes

3.4.1.1. Macropores

It means the pore width is bigger than 50 nm. Macropore distribution can be analysed by mercury porosimetry, but this method has not been used for PS, probably because it requires a relatively large porous volume. The pore dimensions are in that range which can be investigated by electron microscopy, and this is the only technique which can be used.

3.4.1.2. Mesopores (2 -50 nm)

The vast majority of electrochemically etched luminescent material studied to date is mesoporous. Electron microscopy can still be used, but TEM or high resolution SEM analysis are required.

3.4.1.3. Micropores

Wholly microporous material formation is restricted to anodisation in highly concentrated aqueous HF. Such freshly etched layers typically contain supermicropores (1-2 nm width) which could became ultramicropores (<2 nm) after oxidation. The determination of pore size distribution in the range of micropores is very difficult. The radii of the micropores are below 1 nm.

3.5. Fabrication of PS

3.5.1. Formation mechanism

PS is a low dense material, which is produced by an anodic reaction of Silicon in hydrofluoric acid solution. In general, constant current is preferable, because it allows a better control of both the porosity and the thickness. So, the process is regulated by potential between silicon surface and the solution and the ion transport. The simplest cell which can be used to anodise is shown in Fig.2. The silicon wafer serves as anode. The cathode is made of platinum or any acid-resistant material. The cell is generally made of highly acid-resistant polymer such as Teflon.

Anodising equipment

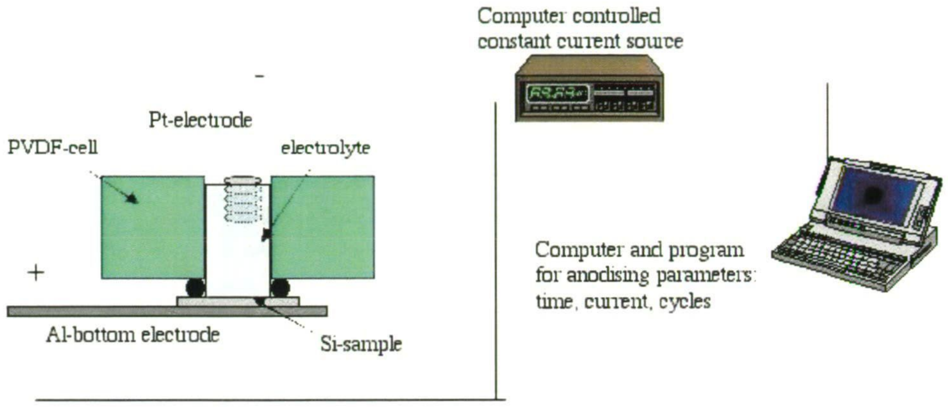

Fig.2. The anodising equipment used in our experiments.

PS consists of very fine through holes and residual silicon region (Figs.3. and 4.). Generally, the diameters of the holes are about several nanometers. The process of the nano-hole formation is a sort of self-organising solving reaction of silicon atoms into hydrofluoric acid. In spite of its nanostructure and therefore its large surface area, the formation of PS proceeds quite uniformly over the hole sample and reproducible with adequate control of anodisation current density, the concentration of hydrofluoric acid and the resistivity of silicon substrate.

Various models have been applied to try and explain the rich variety of PS structures formed by electrochemical etching of crystalline silicon in hydrofluoric acid. The selective dissolution process occurs at the anodisation of the silicon wafer and is related to the mechanism of the charge transfer at the silicon interface controlled by constant current or constant voltage. There is a critical value of the current density beyond which the PS formation stops and the electropolishing process begins. PS consists in an array of pores penetrating into silicon substrate, surrounded by silicon skeletons.

Because of these deep pores it has a very large specific surface.

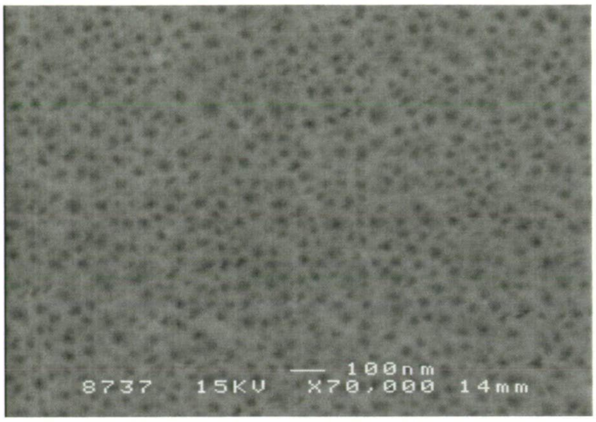

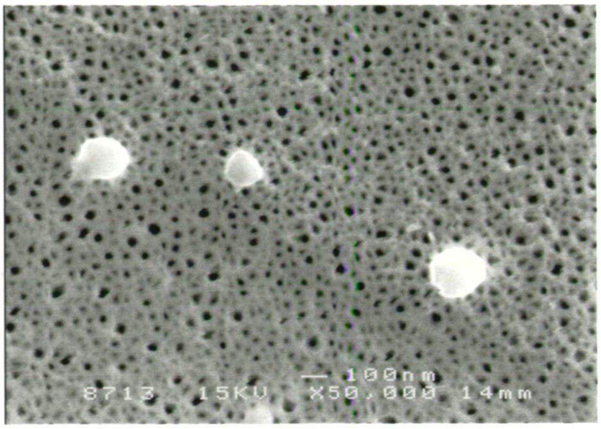

Fig. 3. Typical mesoporous silicon surface. Fig.4. On the porous surface, the spheres are supposed to be SiO_2 or CuO (It's only assumption) in the range of hundreds of nanometers.

3.5.1.1. Chemical background of the formation mechanisms of PS

Several models have been created in order to find explanation of the pore formation in Si during electrolytic treatment in HF based solutions. In some works, authors concluded that the reaction is initiated at the defects (cracks, impurities, dislocations) of the Si surface [1-2]. In others, the pore nucleation was attributed to the instability of the planar Si surface in the electrolyte [3-5]. Although, the chemistry of the Si dissolution during the anodisation process is not evidenced, some possible reaction mechanisms have been proposed:

In Ref. [6], a surface bond oxidation scheme was assumed: (a) A F^--induced nucleofilic attack of the =SiH_2 surface bond can occur, when a h^+ hole reaches the surface yielding a =SiHF bond. (b) An another F^-attack on the same Si causes an e-injection into the substrate and results in H_2 generation and =SiF_2 formation (c) Because of the high electronegativity of fluorine -the novel =SiF2 group operates as an electron acceptor – the electron density of Si-Si bond is lowered and these weakened Si-Si bonds can be attacked by HF and H2O yielding a leaving SiF4 molecule and novel =SiH_2 bonds, respectively.

Other authors showed another alternative way for the HF-assisted dissolution of positively biased Si [7]. The idea is a multi-step reaction. (a) In the first the Si is oxidised by holes ($Si + 2\,h^+ \rightarrow Si^{2+}$) and dissolved into the electrolyte-substrate interface as $[SiF4]^{2-}$complex. In the next step two possible reactions can run parallel both in the solution and (in case of adsorbed complexes) on the surface: (b1) oxidation of Si^{2+} ions by protons of the electrolyte ($Si^{2+} + 2\,H^+ \rightarrow Si^{4+}$) and (b2) disproportion of $^{2+}$ ions forming Si and Si^{4+} ions ($2\,Si^{2+} \rightarrow Si + Si^{4+}$). Owing to the secondary Si formation, this dissolution model can also account for the evolution of both the micro- and nanopores.

3.6. Manufacturing of PS; porosity and thickness dependence on electrolyte composition

PS layers were manufactured by the anodisation of silicon (Si) wafers in hydrofluoric acid/ethanol/water ($HF/EtOH/H_2O$) and hydrofluoric acid/surfactant/water ($HF/Decon/H_2O$) electrolytes. Physical parameters such as thickness (d) and porosity (p) of the formed PS were determined as the function of concentrations of HF, EtOH, Decon ([HF], [EtOH] and [Decon], respectively). It was found that higher [HF] decreases, while higher [EtOH] increases the porosity and helps to produce both uniform anodisation and PS layers. The thickness of the formed PS films were measured by profilometry and proved to be proportional to [HF] and inversely proportional to [EtOH].

Recently, PS has been a widely studied material owing to its possible applications in optics [8,9], optoelectronics [10,11], sensors [12,13] and quantum electronics [10,14,15]. Several detailed papers have already been published concerning the formation [16,17], and the physical-chemical properties of PS [18]. In general, the papers have not dealt with the dependence of the process and the properties of manufactured PS upon the concentration of the components in the electrolyte. Since the most important parameters of the PS layers are its porosity and thickness, our investigations were focused on how these properties change on varying the composition of the electrolyte. In this chapter, the dependence of these parameters on the concentration of the electrolyte is presented.

3.6.1. Experimental and discussion

The PS layers were made in darkness by electrochemical etching of p-type, boron doped, Si wafers (with resistivity of 0.015 Ωcm) in HF/EtOH and HF/Decon based electrolytes. During the anodisation process, current density (50 mA/cm^2) and etching time (200 s) were adjusted to be constant values using a computer controlled anodisation cell. The cell was made of PVDF and platinum was used as a cathode. In each experiment the total volume of the electrolyte was 5 ml. The stripping of the anodized samples – for the thickness and porosity measurements -was carried out in 1 M NaOH aqueous solution. The prepared PS samples were rinsed in EtOH and stored in pentane in order to prevent oxidising and cracking.

The porosity is defined and calculated as the fraction of void within the PS layer and can be determined by weight measurements: p(%) = (m1-m2)/(m1-m3), where m1, m2 and m3 denote the mass of the original-, anodized-and stripped wafer, respectively. The thickness of the formed PS films was determined by profilometry followed by stripping.

3.6.1.1. The HF/EtOH/H_2O system:

In addition to HF, water and EtOH were added to the solution. In order to measure the effect of the electrolyte composition on the thickness and porosity of the silicon layer, the volume of one component was kept constant while the others were varied. Both the thickness (Fig.5.) and porosity (Fig.6.) values were dependent on the concentration of EtOH and HF.

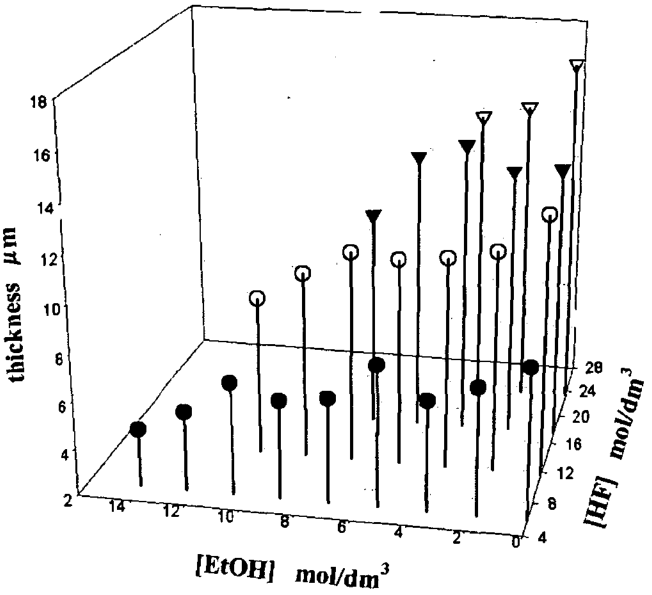

Fig.5. Thickness of the porous layer vs. the concentration of EtOH and HF. The parameters of the anodisation were constant (200 s and 50 mA/cm^2).

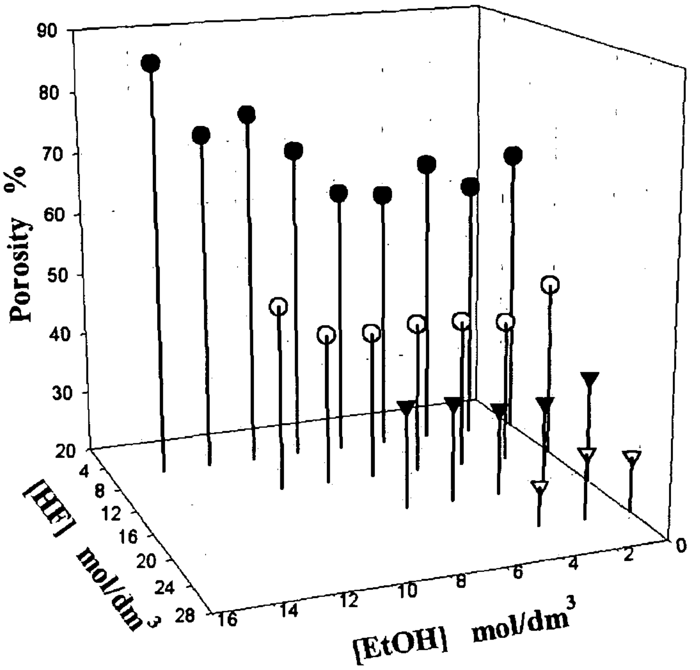

Fig.6. Porosity of the porous layer vs. the concentration of EtOH and HF. The parameters were constant (200 s and 50 mA/cm^2).

By lowering the [HF], the porosity of the substrate is raised until there is enough HF serving F^--ions in the electrolyte. This is necessary to oxidise Si and provide charge carriers for the electrolysis. When the HF content was reduced below 2 M, the constant 50 mA/cm^2 current density could not be supplied at reasonable voltage and thus the attempt to prepare PS failed. For a given concentration (10 M < [HF] < 29 M) there is no significant change in the porosity with respect to the concentration of EtOH. However, in the case of lower ([HF] <10 M) HF content, porosity slightly increases (from 60% up to 90%) with increased EtOH content of the electrolyte (3.5 M < [EtOH] <14 M). In order to fabricate samples with the highest porosity (p > 60%), the optimal concentration values of HF and EtOH were determined to be 4 M ± 2 M and 12 M ± 2 M, respectively (Fig.7.).

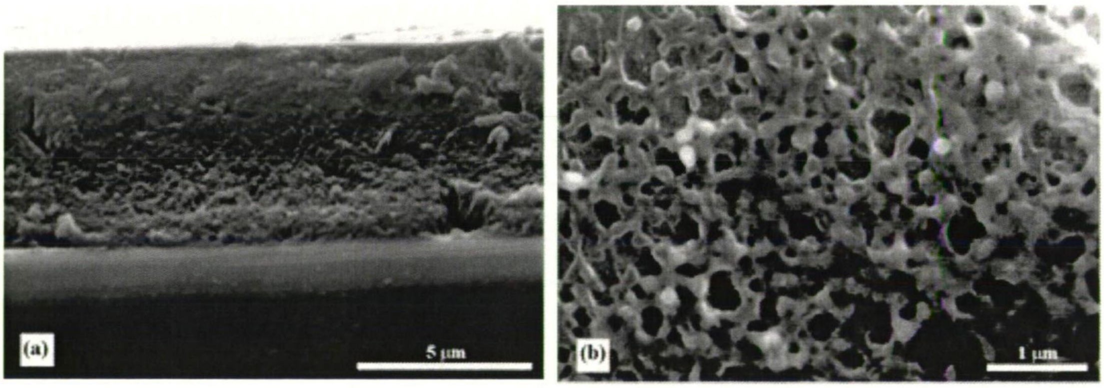

Fig.7. a. Low magnification FESEM image of a cross-section of high porosity Silicon layer. Fig 7. b. shows a high magnification picture taken from the porous part. The anodisation was carried out by using a solution of 14 M EtOH, 6 M HF.

The thickness of the formed PS layers can be seen in Fig.6. as a function of the composition of the electrolyte. It appears that increasing the concentration of HF causes thicker PS. In many publications [9-11], it is concluded that the chemical mechanism of the anodisation has no direct dependence on EtOH content of the electrolyte. Our measurements show a moderate decrement of thickness with increased [EtOH], probably caused by the decreased activity of F^--ions in the EtOH based electrolyte. It is also known that the role of EtOH during the process is only physical, namely it lowers the surface tension of the electrolyte. This is important because vigorous hydrogen bubble formation can be observed during the process. Higher [EtOH] prompts the bubbles to detach from the interface due to the reduction of surface tension. This means that the bubbles formed on the surface of Si do not disturb the transport of ions towards and away from the substrate/electrolyte interface, resulting in a homogenous and uniform anodisation and PS generation.

3.6.1.2. The HF/Decon/H_2O system

In a parallel experimental series, EtOH was changed for a commercially available surfactant (Decon 90®). At first -in order to perform fast anodisation -[HF] was held at a constant high value ([HF] = 23 M) and the concentration of the surfactant was varied (the volume ratios of Decon were adjusted to be 1/5, 1/50, 1/500, 1/5000, and 1/50000). The thickness of PS formed in this way was close (d ~ 15 μm) to the corresponding solution containing EtOH. Concerning the porosity, the effect of the surfactant content was not as significant as in the case of EtOH in the HF/EtOH/H_2O system. A tenfold concentration increment of surfactant resulted in ~3 % of additional porosity, thus a maximum porosity of 40 % could be reached when 1 ml pure Decon was added to the 4 ml HF.

On the other hand, when the experiments were repeated with diluted HF ([HF] = 6 M) the results we obtained were similar to the previous case of the HF/EtOH/H_2O system regarding the thickness (d ~ 7 μm) and uniformity. However, this was significantly different relating to the porosity. Namely, the porosity has not become as high as in the HF/EtOH/H_2O system with the reduced [HF] even though the surface tension of the solution was reduced because of the high amount of surfactant. The highest porosity was measured to be 67 %, contrary to the 90 % achieved in the HF/EtOH/H_2O system. It can also be concluded that the porosity has not been affected drastically by the surfactant when its volume ratio was between 1/5 and 1/5000 but dropped below 50 % when 1/50000 dilution was employed.

3.7. Conclusions of chapter 3.

In this chapter, we demonstrated the effect of the electrolyte composition (concentration values of HF, EtOH, Decon) on PS formation (thickness, porosity) in the anodisation procedure. In the HF/EtOH/H_2O system, the porosity was increased with reduced [HF] and with elevated [EtOH]. The thickness increased with higher [HF] but decreased when [EtOH] was raised. When a commercial surfactant was applied in the electrolyte instead of EtOH, the porosity could not be increased beyond 70 %. However the thickness values were analogue to the results we acquired in that case when the electrolyte contained EtOH. In general, it can be claimed that the uniformity of PS layers can be advantageously influenced by applying higher [EtOH] or [Decon].

References of chapter 3.:

1. Silicon, Collection of Articles, Ed. By D.A. Petrov (inostrannaya Literatura, Moscow, 1960).
2. P. Allongue, V. Costa-Keiling, and H. Gerisher, J. Electrochem. Soc. 140, 1009 (1993).
3. Y. Kang and J. Jorré, J. Electrochem. Soc. 140, 2258 (1993).
4. A. Valance, Phys. Rev. B 52, 8323 (1995).
5. A. Valance, Phys. Rev. B 55, 9706 (1997).
6. V. Lehmann and U. Gösele, Appl. Phys. Lett. 58, 856 (1991).
7. D.N. Goryachev, L.V. Belyakov, and O.M. Sreseli, Semiconductors 34, 1090 (2000).
8. Thönissen, M. Krüger, G. Lerondel, R. Romestain, Properties of Porous Silicon, ed. by L. Canham) published by INSPEC (1997) 349-355.
9. W. Theiβ, Surf. Sci. Reports 29(1997) 91-192 (and references there in).
10. O. Bisi, S. Ossicini, L. Pavesi, Surf. Sci. Reports 38(2000) 1-126 (and references there in)
11. A.G. Cullis, L.T. Canham, P.D.J. Calcott, J. Appl. Phys. 82(1997) 909-965
12. A. Foucaran, B. Sorli, M. Garcia, F. Pascal-Delannoy, A Giani, A. Boyer, Sensors and Actuators 79(2000) 189-193.
13. V. Mulloni, L. Pavesi, Appl. Phys. Lett. 76(2000) 2523-2525.
14. S. Gardelis, J.S. Rimmer, P. Dawson, B. Hamilton, R.A. Kubiak, T.E. Whall, E.H.C. Parker, Appl. Phys. Lett. 59(1991) 2118-2120.
15. A.J. Read, R.J. Needs, K.J. Nash, L.T. Canham, P.D.J. Calcott, A. Qteish, Phys. Rew. Lett. 69(1992) 1232-1235.
16. V. Lehmann and U. Gösele, Appl. Phys. Lett. 58, 856 (1991).
17. D.N. Goryachev, L.V. Belyakov, and O.M. Sreseli, Semiconductors 34, 1090 (2000).

4. THE VANADIUM OXIDES AND PULSED LASER DEPOSITION

The principal oxides of vanadium occur as single valency oxides in the oxidation states from V^{2+} to V^{5+}, which is in form of VO, V_2O_3, VO_2, and V_2O_5. However, the vanadium–oxygen phase diagram also includes mixed valency oxides containing two oxidation states, such as V_6O_{13} with V^{5+} and V^{4+} and a series of oxides between VO_2 and V_2O_3 (e.g. V_8O_{15}, V_7O_{13}, V_6O_{11}, etc.), which contain V^{4+} and V^{3+} species.
These mixed valency oxides are formed by introducing oxygen vacancy defects into the respective higher oxides. If the number of oxygen vacancies exceeds a certain value, the vacancies tend to correlate and form the so-called crystallographic shear planes, i.e. the vacancies associate along a lattice plane and become subsequently eliminated by reorganisation of V-O coordination units. The result is a series of oxides with related stoichiometries, such as the Magnéli phases with V_nO_{2n-1} or the Wadsley phases with $V_{2n}O_{5n-2}$ formulas [14].

4.1. The crystal structure and the utility of V_2O_5

V_2O_5 is the most saturated (highest oxidation state) oxide and therefore the most stable one in the V-O system. It crystallizes with an orthorhombic unit cell structure belonging to P_{mnm} space group with lattice parameters of a = 11.510 Å, b = 3.563 Å and c = 4.369 Å. It has a layer-like structure and it is built up from distorted trigonal bipyramidal coordination polyhedra of O atoms around V atoms, that share edges to form $(V_2O_4)_n$ zigzag double chains along the (001) direction and are cross linked along (100) through shared corners as shown in Fig.1. The distorted polyhedra have a short vanadyl bond (1.58 Å) and four O atoms located in the basal plane at distances ranging from 1.78 to 2.02 Å. The sixth O atom in the coordination polyhedra of V lies along the vertical axis opposite to the V-O bond at a distance of 2.79 Å [11].
From chemical point of view, V_2O_5 is an excellent catalyst [13] due to its rich and diverse chemistry that is based on two factors, namely the variety of vanadium oxidation states, ranging from 2^+ to 5^+, and the variability of oxygen coordination geometries. This structural richness is the source for the existence of differently coordinated oxygen ions, which provide an important ingredient for the physical and chemical surface properties [14].

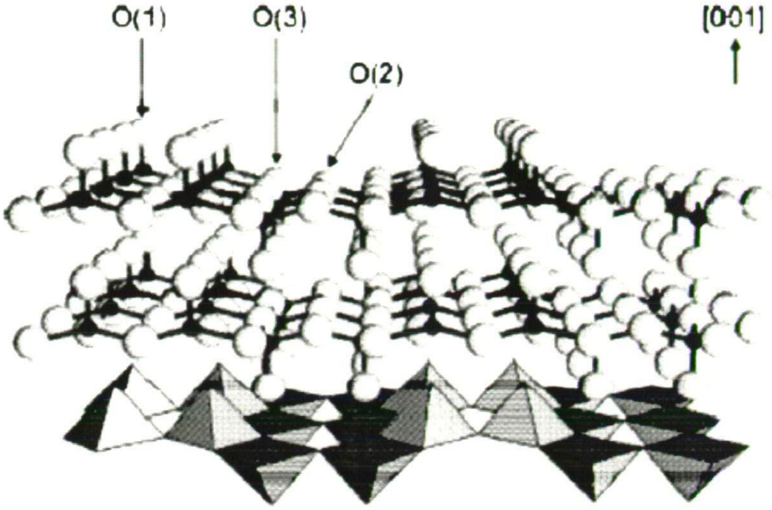

Fig.1. Perspective view of three layers of V_2O_5 with an exposed (0 0 1) surface (V atoms dark balls, O atoms light balls: weak van der Waals bonds omitted for clarity). In the third layer the corner- and edgesharing VO_5 space pyramids are shown.

Among transition metal oxides (WO_3, MoO_3), V_2O_5 has drawn significant interest due to its industrial applications in optical switching devices [1], electrochromic devices [2] and reversible cathode materials for Li batteries [3-6]. V_2O_5 thin films have been already prepared by various methods on different substrates including sol-gel technique [7,8], electron beam evaporation [9], magnetron sputtering [10,11], pulsed laser deposition (PLD) [12].

Since PLD is an excellent method for the fabrication of clusters in the nanoscale range, in this chapter, we present experimental results of nanocrystalline V_2O_5 films synthesized by ArF* excimer laser with a constant 220 °C deposition temperature with recourse of the energy density of the laser beam and the number of pulses.

4.2. Experimental procedures and PLD setup

High-purity (99.99 %, ordered from Aldrich) V_2O_3 powder was subjected to a pressure of $2x10^9$ Pa to form pellets of 13 mm in diameter and 4 mm in thickness. Before irradiation, the pellets were annealed at 550 °C in air for 24 hours. It's worth noting the coloration of the pellets from dark blue to orange, which exhibits the transition of $V_2O_3 \rightarrow V_2O_5$.

PLD was performed in a stainless steel vacuum chamber evacuated by a turbomolecular pump. Schematic representation can be seen in Fig.2. A fused silica glass substrate was placed in front of the target equipped with a heater, allowing the variation of the substrate temperature in the range of 200-400 °C. Target – substrate distance was about 5 cm. A continuous flux of oxygen was introduced into the chamber after pumping down the pressure to about 1.33 x 10^{-5} Pa.

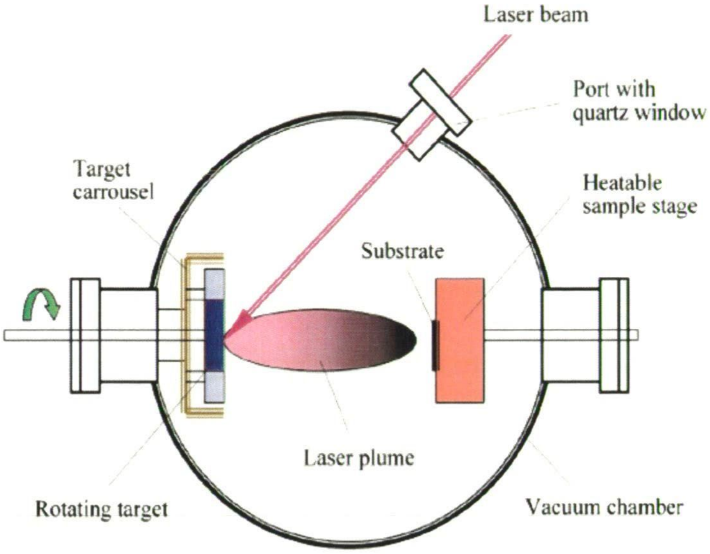

Fig.2. Typical set-up arrangement for pulsed laser ablation from Ref. [31].

The targets were ablated by a pulsed ArF* excimer laser (λ=193 nm, pulse duration 15 ns at FWHM) at a fluence level of 0.9-2.7 J/cm^2. Repetition rate was 2 Hz. The laser beam was focused onto the target with an incident angle of 45°. The target was rotated by an electric motor to avoid the depletion at any spot.

The laser induced coloration of V_2O_5 must be mentioned, i.e. the colour of the surface of V_2O_5 target immediately turned deep blue upon the ablation of the ArF* excimer laser. As it was reported in Ref.[15], this phenomenon is due to photocromism and also the sub-stoichiometry caused by the laser irradiation.

4.3. Results and Discussion

4.3.1. X-ray diffraction measurements

Fig.3.a. shows a set of XRD patterns of V_2O_5 films deposited in O_2 partial pressure of 13.33 Pa with varying the fluence. These patterns reveal the polycrystalline structure of the films deposited at temperature as low as 220 °C. Moreover it shows the predominant (001) peak of orthorhombic V_2O_5 phase. However, the fact, that V_2O_5 is polycrystalline at this deposition temperature is one of the main advantages of PLD compared to other physical vapor deposition methods such as electron-beam evaporation and sputtering, the reported deposition temperature were in the range of 300-500 °C. For example, Kumar et al. reported amorphous structure at 300 °C using vacuum evaporation technique [17]. This lower temperature of crystallization in case of PLD can be explained by the high kinetic energy (>1 eV) of the ejected species in the laser produced plasma. The condensed particles have high energies after being deposited. The ad-atom mobility is able to produce highly oriented nano-crystalline films even at low temperature.

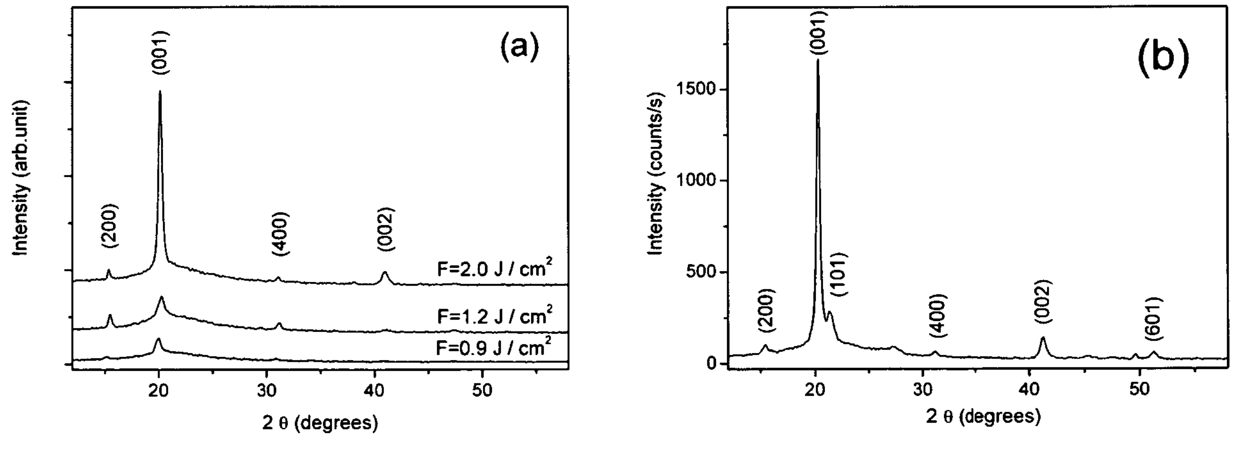

Fig.3.a. X-ray diffraction patterns of V_2O_5 films deposited at various fluences in O_2 partial pressure of 13.33 Pa at T_s=220 °C (6000 pulses). Fig 3.b. V_2O_5 produced by 15000 pulses and F = 2.7 J/cm^2 at 220 °C.

From XRD measurements it can be concluded that each oxide films have nanocrystalline structure. The peaks located at $2\theta \approx 20.2°$, 21.5°, 41° assume the orthorhombic V_2O_5 phase. They are assigned to the (001), (101) and (002) reflections, respectively. It is observed that peaks become narrower with higher intensities by increasing the laser energy density. Consequently, using higher fluences larger clusters were obtained. At the same time we can draw the conclusion that in case of low fluences films become more amorphous. As (002) peak is not present in case of VOa, we are confined to measure the crystallite size in the Transmission electron microscopy images.

Fig.3.b. shows an XRD pattern when using a fluence of 2.7 J/cm^2 and 15000 pulses. We can also conclude that higher energy densities and using more pulses yield more crystallized film.

The calculated cluster sizes are shown in Table.1. The diameters of the V_2O_5 clusters were around 20 nm. It must be noted that these size values correspond to an average crystallite size on the spot where the X-ray passed through.

Name of the sample	Fluence (J/cm^2)	Intensity (W/cm^2)	Number of pulses	Mean cluster size calculated from XRD, D (nm)
VOa	0.9	60×10^6	6000	-
VOb	1.2	80×10^6	6000	18.7
VOc	2.0	133×10^6	6000	21.5
VOd	2.7	180×10^6	15000	21.8

Table 1. Cluster sizes in the function of fluence and number of pulses.

4.3.2. Optical transmission and band gap calculations

The variation in spectral transmittance (T) as a function of the fluence is shown in Fig.4. It is clearly seen that using higher fluence, thicker film can be obtained, i.e T decreases with higher fluence. Interesting to see the peak around 330 nm indicating that the films are non homogenous and lower oxidation states of vanadium are also present. Thus, we can conclude that the films are in multiphase forms as it is reported also in other works in case of vanadium oxide films thinner than 400 nm [18]. This transmission peak phenomenon has not been explained elsewhere.

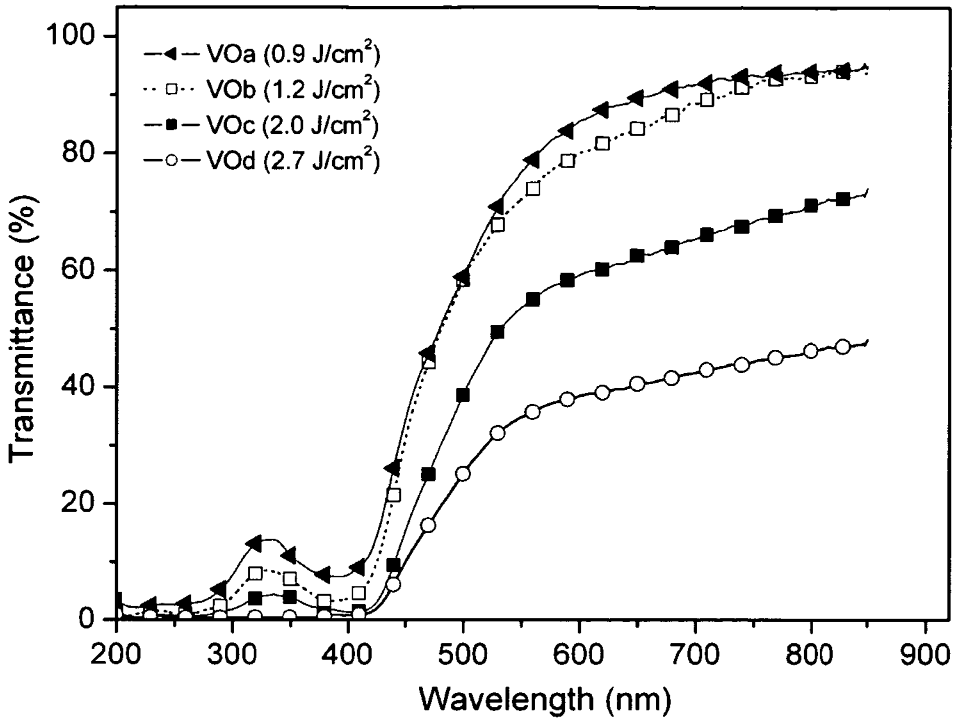

Fig.4. Optical transmission characteristics of V_2O_5 thin films formed at 220 °C as a function of different fluences in case of 6000 pulses. VOd shows the optical transmission by using 15000 pulses at a fluence of 2.7 J/cm^2.

Determining the fundamental absorption edge from T measurements, the following expression can be used:

$$\alpha (h \nu) = B (h \nu - E_g)^n \qquad (1)$$

where α is the optical absorption coefficient, hν is the incident photon energy, B is a constant called edge width parameter, E_g is the optical band gap of the material and n is the exponent, that determines the type of electronic transition causing the absorption. It can take values of (1/2) for direct allowed, (3/2) for direct forbidden, 2 for indirect allowed and 3 for indirect forbidden transitions [19]. Normally, α can be calculated by using the relation:

$$\alpha = \{1 / t\} \ln \{ T / (1-R)^2 \} \qquad (2)$$

where T is the transmittance, R is the reflectance and t is the thickness of the film. In case of thin and highly transparent films, R can be considered nearly 0.

Despite the fact that the thickness is unknown in our case, we can deduce the value of the absorption edge by using the Tauc plot since the thickness depends only on laser fluence and the number of pulses. Consequently, we can plot $\alpha\, t\, h\nu$ vs. $h\nu$ (Fig.5.), where t means a constant multiplier that does not influence the evaluation of the optical band gap. The optical band gap can be evaluated by extrapolating the linear region of the plot to zero ($\alpha = 0$).

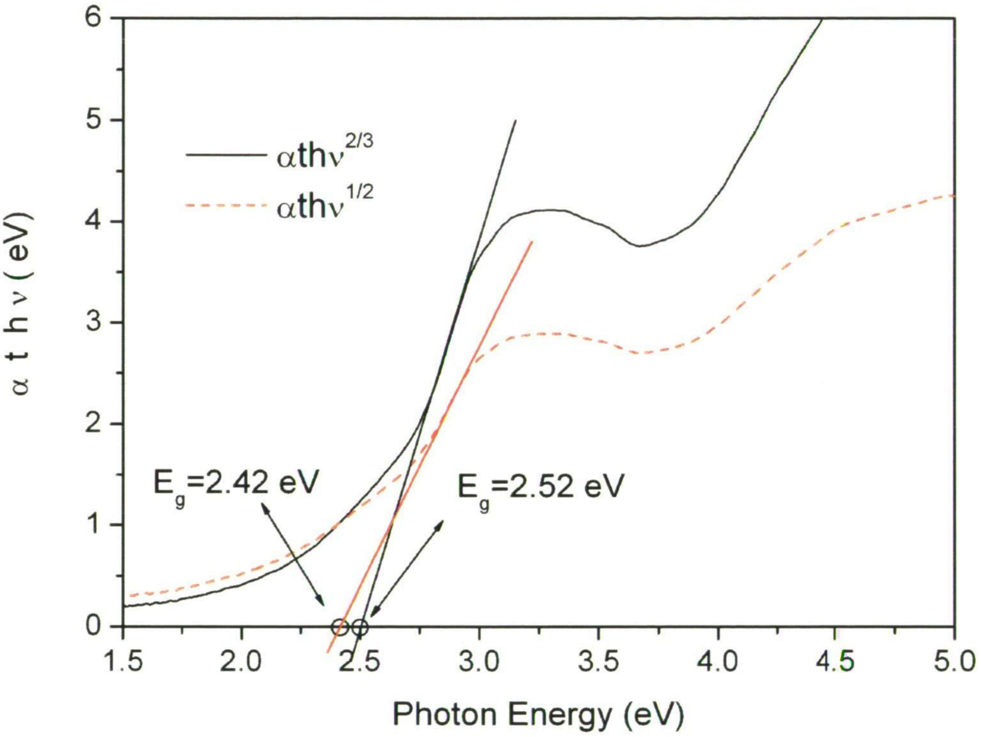

Fig.5. $\alpha t\, h\nu$ vs. $h\nu$ plots for V_2O_5 thin film (VOc).

As it is shown in Fig.5., both the 1/2 (indirect allowed) and the 2/3 (direct forbidden) fits give similar result for the absorption edge, but 2/3 is preferred as it gives a better fit. The calculated optical band gaps for VOb and VOc are 2.53 eV and 2.52 eV, respectively.

Both types of transitions have already been reported [19,20]. For example, in case of single crystals of V_2O_5, Bodó and Hevesi [21] and Kenny et al. [22] reported that α varies linearly with $(h\nu)^{3/2}$ which is characteristic of direct forbidden transition across the band gap of a crystalline solid.

The calculated optical band gaps were around 2.5 eV for V_2O_5, which is in good agreement with vanadium oxide films thinner than 400 nm [18].

4.3.3. X-ray photoelectron spectroscopy

High resolution XPS were acquired in the binding energy range of 510-540 eV (Fig.6.) .The recorded XP spectra show three intensive peaks corresponding to the core level binding energies of O (1s), V ($2p_{1/2}$) and V ($2p_{3/2}$), respectively. The main signal of the O (1s) spectrum has a binding energy at about 530 eV.

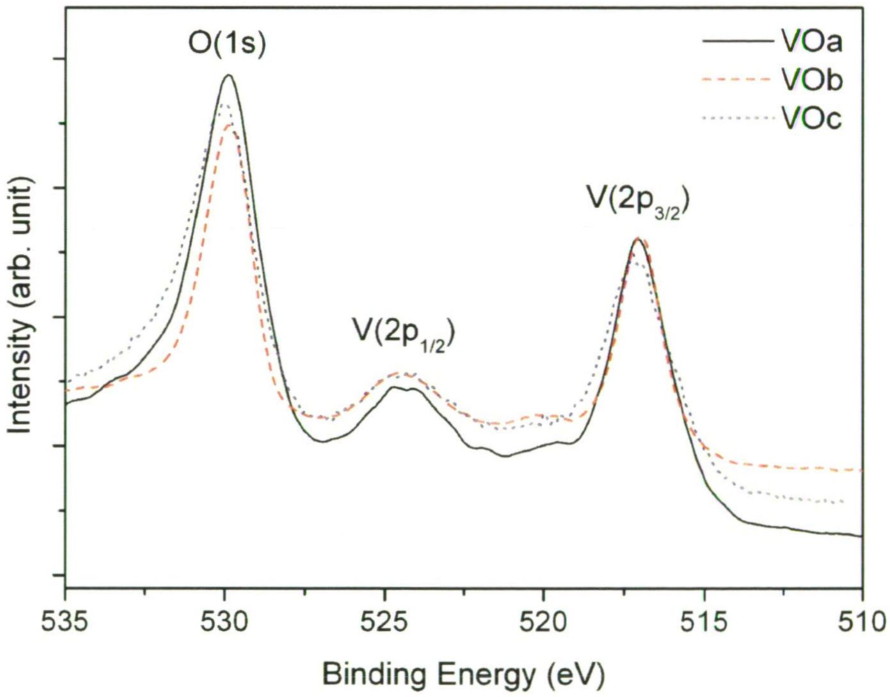

Fig.6. X-ray photoelectron spectra of different V_2O_5 films prepared by using 6000 pulses with fluence varying from 0.9 to 2.0 J/cm^2.

The typical spin-orbit splitting between V ($2p_{3/2}$) and V ($2p_{1/2}$) peaks for all the films deposited at different fluences is about 7.2 eV. This value is in good agreement with the previous works [23].

The core level binding energy peaks, namely V(2p) and O(1s), are used to characterize the chemical state of vanadium in V_2O_5 films. Binding energies, their chemical shifts and FWHMs are used for the analysis. There is a relationship between the core level binding energy and the charge state associated with an individual atom. An increase in the core level binding energy indicates an increase in the positive charge of the atom [24]. The core level binding of the $V(2p_{3/2})$ emission energy in metallic vanadium is 512.4 eV [25]. For polycrystalline, stoichiometric V_2O_5, the $V(2p_{3/2})$ peak position was reported at 517.0 eV with a chemical shift of 4.6 eV characterizing the highest oxidation state of vanadium [26]. The FWHM of $V(2p_{1/2})$ is much broader than that of $V(2p_{3/2})$ due to the Coster-Kronig Auger transitions [27].

The calculated values and comparison with other works are listed in Table 2.

Sample name and other works	$V(2p_{3/2})$		O (1s)		O/V
	BE (eV)	FWHM(eV)	BE (eV)	FWHM(eV)	
Bulk [26]	517.0	-	529.8	-	-
Films [24]	516.8	2.1	529.6	2.3	2.41±0.05
Pellet [24]	517.0	2.3	529.7	2.6	2.46±0.04
Films [29]	516.9	2.0	529.8	2.2	2.5±0.2
This work : VOa	517.1	1.7	529.9	2.1	2.41
VOb	517.0	1.5	529.8	1.5	2.38
VOc	517.2	2.1	530.1	2.2	2.50

Table 2. Comparison of binding energies, FWHMs and core level area ratios of V_2O_5 samples.

They are in agreement with those reported for orthorhombic bulk V_2O_5 [19]. Sample stoichiometry ratios $S_{i,j}$ are calculated from the XP spectra using the following formula [28]:

$$S_{i,j} = \frac{C_i}{C_j} = \frac{I_i / ASF_i}{I_j / ASF_j} \qquad (3)$$

where C_i and C_j are the concentrations of the elements, I_i and I_j the background corrected intensities of the photoelectron emission lines and ASF_i and ASF_j the atomic sensitivity factors for photoionization of the i^{th} and j^{th} elements. For example the O to V ratio in stoichiometric V_2O_5 should be $S_{O,V} = 2.5$. This formula is only valid for homogenous element distributions in the sample. The calculated ratios are shown in Table 2.

4.3.4. Transmission electron microscopy

Fig.7. corresponds to sample VOc. Collections of NCs assembled in a continuous layer are observed and we can see that diameters of the NCs varies between 15 and 30 nm.

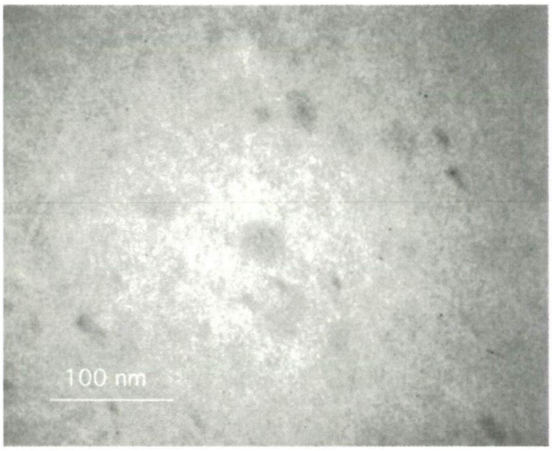

Fig.7. TEM image of VOc produced by high fluence.

On the contrary, as it is shown in Fig.8., when utilizing the lowest fluence (0.9 J/cm^2), most of the NCs are smaller than 5 nm. The size histogram corresponding to this sample (VOa) is shown in Fig.9. The average cluster diameter is about 4 nm.

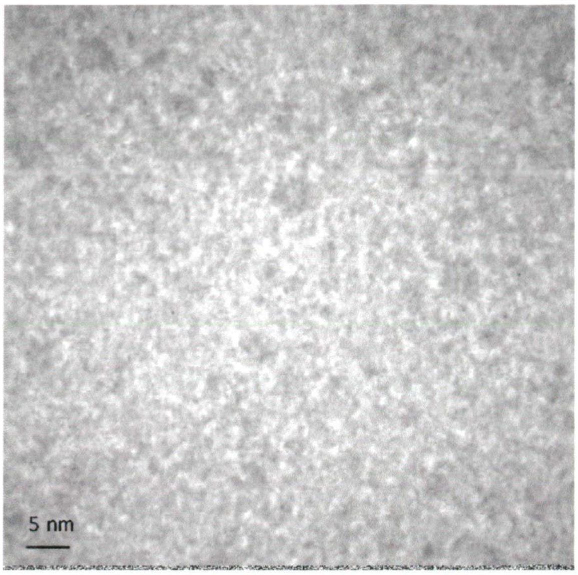

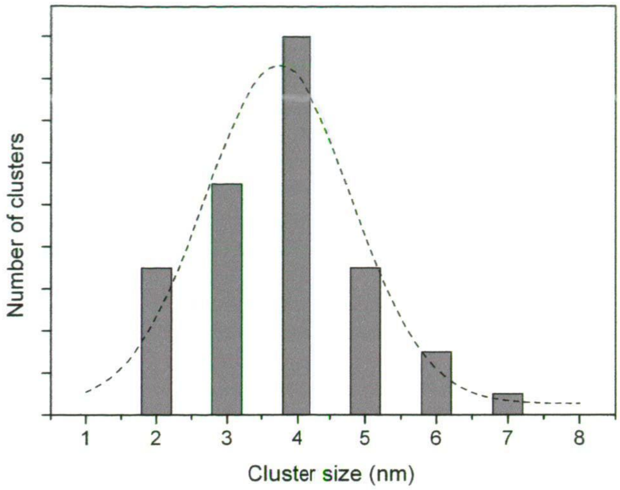

Fig.8. TEM image of VOa produced by the lowest fluence (0,9 J/cm^2) and Fig.9. shows the cluster size distribution of VOa.

Fig.10. shows a large V_2O_3 domain observed along the [110] direction in the VOb sample. The power spectrum of the image is given in the inset. As it was mentioned earlier, during the formation of the vanadium oxide, lower oxides can be created. However, the evolution of V_2O_5 to V_2O_3 during the exposure in the electron beam of the microscope cannot be excluded.

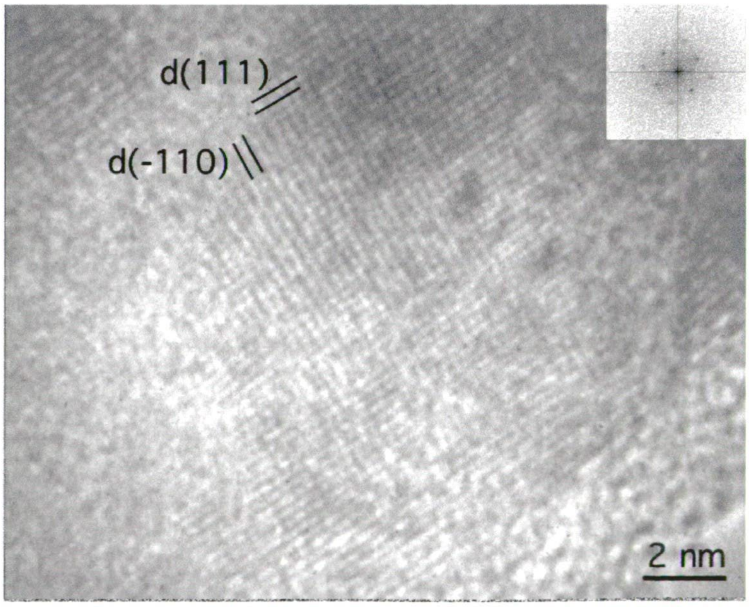

Fig.10. HRTEM image of a crystalline domain with the V_2O_3 stoichiometry observed on the VOb.

HRTEM applied to small pieces of the oxide surfaces is not a statistic technique to determine the structure and orientation of the deposit. However, the TEM observations give more precise measurements of the cluster size according to the fluence and a better description of the polycrystalline layer. The V_2O_3 structure was not detected by X-rays, so that it seems reasonable to believe that the quantity is very low in the sample and it is also produced during the interaction with the electron beam.

4.3.5. Effect of cluster size on the absorption edge

From HRTEM images it is clearly seen that NCs are present in the range of some nanometers. It is well known that due to the quantum confinement effect small sized particles with a diameter below the Bohr radius can give rise to the energy gap of semiconductor materials. For this reason we calculate the Bohr radius for the V_2O_5 using the following equation:

$$a_B = 4\pi\varepsilon_0\hbar^2\varepsilon / e^2 m_0 \mu = 4.52 \text{ nm} \qquad (4)$$

where $\mu = m_e m_h / (m_e + m_h)$ is the reduced exciton mass, m_e (0.24) and m_h (0.5) are the electron and the hole effective masses, respectively. ε_0 and ε are the dielectric constant of the vacuum and the V_2O_5, respectively, e is the elementary charge [30].

As the calculated Bohr radius (4) is about 4.5 nm and the dimensions of some clusters are below this value, these grains can give rise to the energy gap yielding a blue shift in the absorption edge. We assume, from the TEM observations, that the presence of these lower sized (<4.52 nm) NCs contribute to the shift of the band gap value related to the one of the bulk material (2.25 eV).

4.4. Conclusions of chapter 4.

We have synthesized highly oriented nanocrystalline V_2O_5 films by PLD using different fluences and pulse numbers. From HRTEM images we can conclude that the size of NCs are in the range of 2-40 nm. From experimental results it is evident that NC size depends on the laser fluence used during deposition. Consequently, NC size can be selected by adjusting the laser fluence.

We estimated the optical band gap to be about 2.52 eV and we determined the Bohr radius to be 4.52 for V_2O_5. We observed the shift of the absorption edge relating to the bulk value. We assume that the shift of the edge relies on two facts. Firstly, a part of NCs with diameters inferior to Bohr radius, increase the energy gap. Secondly, during the formation of V_2O_5 thin films, lower oxidation states of vanadium are also created that give rise to the energy gap. These two effects together influence the band gap and yield a relatively high value.

References of chapter 4.:

1. J.B. Goodenough, Solid State Chem. 5 (1971) 45.
2. D. Wruck, S. Ramamurthi, M. Rubin, Thin Solid Films 182 (1989) 79.
3. A. Süli, M.I. Török, I. Hevesi, Thin Solid Films 139 (1986) 233.
4. J.G. Zhang, J.M. McGraw, J.Turner, David Ginley, J. Electrochem. Soc. 144 (1997) 1630.
5. C. Julien, B. Yebka, J.P. Guesdon, Ionics 4 (1995) 316.
6. C. Julien, E. Haro-Poniatowski, M. A. Camacho-López, L. Escobar-Alarcón and J. Jímenez-Jarquín, Mat. Sci. Eng. B 65 (1999) 170.
7. N.Özer, Thin Solid films 305 (1997) 80.
8. S. Beke, L. Kőrösi, S. Papp, L. Nánai, A. Oszkó, J.G. Kiss and V. Safarov, Appl. Surf. Sci. (to be published)
9. C.V. Ramana, O.M. Hussain, B. Srinivasulu Naidu and P.J. Reddy, Thin Solid Films 305 (1997) 219.
10. M. Ghanashyam Krishna and A.K. Bhattacharya, Mat. Sci. Eng. B 49 (1997) 166.
11. W. Gulbinski, T. Suszko and D. Pailharey, Wear 254 (2003) 988.
12. C.V. Ramana, R.J. Smith, O.M. Hussain, Phys. Stat. Sol. 1999 (2003) R4
13. B.M. Weckhuysen, D.E. Keller, Catal. Today 78 (2003) 25.
14. S. Surnev, M. G. Ramsey and F. P. Netzer, Surf. Sci. 73 (2003) 117.
15. Z. Liu, G. Fang, Y. Wang, Y. Bai, K.-L. Yao, J. Phys. D: Appl. Phys. 33 (2000) 2327.
16. E.F. Kaelbe, Handbook of X-Rays, McGraw-Hill, New York, 1967
17. R.T. Rajendra Kumar, B. Karunagaran, V. Senthil Kumar, Y.L. Jeyachandran, D. Mangalaraj, Sa. K. Narayandass, Mat. Sci. in Semicond. Proc. 6 (2003) 543.
18. M. Ghanashyam Krishna, Y. Debauge, A.K. Bhattacharya, Thin Solid Films 312 (1998) 116.
19. C.V. Ramana, O.M. Hussain, S. Uthanna, B. Srinivasulu Naidu, Opt. Mat. 10 (1998) 101.
20. M. Ghanashyam Krishna, A. K. Bhattacharya, Mat. Sci. Eng. B 86 (2001) 41.
21. Z. Bodó, I. Hevesi, Phys. Stat. Sol. 20 (1967) K45.
22. N. Kenny, C.R. Kannewurf, D. H. Whitmore, J. Phys. Chem. Solids 27 (1966) 1237.
23. K.Wandelt, Surf. Sci. Rep. 2 (1982) 1.
24. A.Z. Moshfegh, A. Ignatiev, Thin Solid Films 198 (1991) 251.

25. R. Larsson, B. Folkesson, G. Schön, Chem. Scr. 3 (1973) 88.
26. R.J. Colton, A.M. Guzman, J.W. Rabalais, J. Appl. Phys. 49 (1978) 409.
27. E. Antonides, E.C. Janse, G.A. Sawatzky, Phys. Rev. B 15 (1977) 4596.
28. C.D. Wagner, W.M. Riggs, L.E. Davis, J.F. Moulder, Handbook of X-ray Photoelectron Spectroscopy, Perkin Elmer Corporation, Eden Prairie, 1979
29. C. V Ramana, O. M. Hussain, B. Srinivasulu Naidu, C. Julien and M. Balkanski, Mat. Sci. Eng. B 52 (1998) 32.
30. G.V. Samsonov, The Oxide Handbook, Institute of Problems in Materials Science, Academy of Sciences of the Ukrainian SSR, Kiev, 1973
31. http://superconductivity.et.anl.gov/Techniques/PLD.html

5. ND:YAG LASER SYNTHESIS OF NANOSTRUCTURAL V_2O_5 FROM VANADIUM OXIDE SOLS

5.1. Laser-assisted surface processing of materials

Surface processing with lasers enables the localized change of composition of materials. Lasers can be used as concentrated light sources to yield a kind of miniaturized chemical reactor in the irradiated volume of the system. Due to the advantageous beam parameters (spatial and temporal coherence, directionality) of lasers the processes can be well directed and monitored, usually with spatial resolution of a micrometer or, in some cases, in the sub-micrometer range. The monochromatic radiation carried out from the IR to the UV regime allows selective excitation of the illuminated molecules and the continuous and pulsed lasers make it possible to have a time-controlled radiation. The laser-matter interaction can cause photolytic (when the thermalization of the absorbed photon energy is slower compared to the rate-determining processing step in a chemical reaction) or otherwise thermal chemical changes. Under appropriate conditions (laser and system parameters), electronic states in the matter are excited, bindings between molecules are opened and a handled surface can be oxidized or reduced [13].

5.2. Experimental procedures

5.2.1. Preparation of $V_2O_5 \cdot nH_2O$ xerogel

V_2O_5 xerogels were prepared by dissolving macrocrystalline V_2O_5 powder (0.1 g) in 30 % hydrogen peroxide (5 ml) at 0 °C. An exothermic reaction took place during a partial decomposition of H_2O_2 leading to the release of O_2 gas. The initially reddish brown suspension firstly became an orange solution and some hours later it turned to a dark red gel.

After the xerogel preparation, 400 μl of gel was dropped onto glass substrate and was dried for some hours in a furnace at about 60 °C. After all, a Nd:Yag (1064 nm) laser beam was focalized on the surface of the sol-gel prepared film to heat locally the selected area. The laser processing was made in air. The experimental setup can be seen in Fig.1.

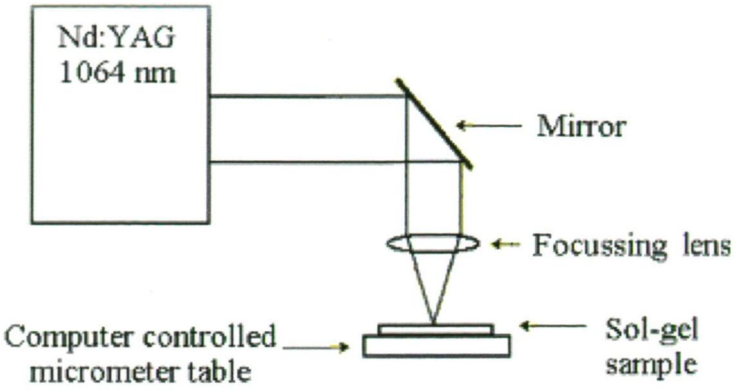

Fig.1. Schematic representation of the experimental set-up for laser treatment of sol-gel samples.

1 cm^2 area was scanned over line per line. As one stripe has a width of about 250-350 μm - depending on the laser intensity-, 4 stripes per mm was scanned on the surface with one repetition to cover the whole area. In Fig.2.a. one stripe can be seen (using an intensity of 102 W/cm^2) and in Fig.2.b. 4 parallel stripes. In this latter, one can see the stripes touch each other therefore most of the area is treated for further analysis.

The irradiated spot size was about 0.00785 cm^2. Scanning speed was set to 0.3846 mm/sec and the intensity of laser radiation was varied in the range of 62-169 W/cm^2.

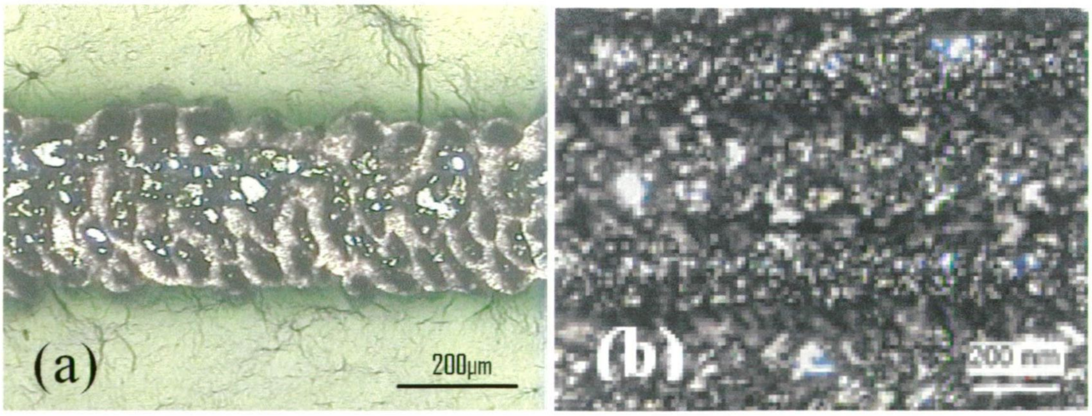

Fig.2.a,b. Optical microscopy images of (a) one stripe and (b) 4 stripes. The laser intensity was 102 W/cm^2 and scan speed was 0,3846 mm/sec with one repetition.

5.2. Results and Discussion

5.2.1. XRD measurements

Fig.3. shows a set of XRD patterns of untreated and laser treated vanadium oxide films with varying the intensity of the Nd:YAG laser. The patterns above 129 W/cm^2 reveal the polycrystalline structure of the films. Moreover, it shows the predominant (001) peak of orthorhombic V_2O_5 phase.

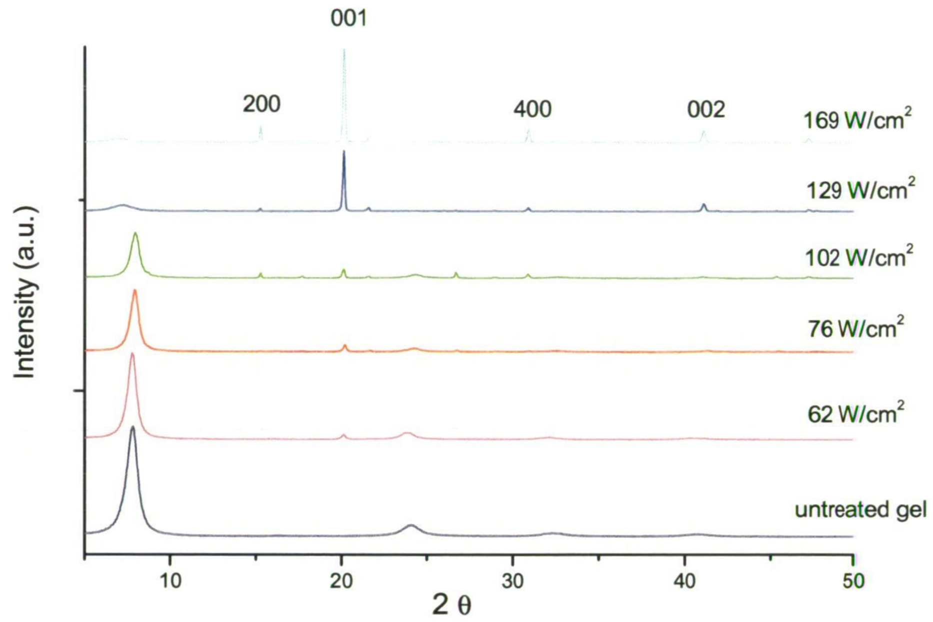

Fig.3. X-ray diffraction patterns of vanadium oxide gel and the irradiated ones by using various intensities in air.

From XRD diffractogram it can be concluded that the peak around the (001) plane is continuously developed by the applied laser beam intensity. In case of using the highest intensity, the peaks located at $2\theta \approx 20.2°$, $21.5°$, $41°$ assume the orthorombic V_2O_5 phase. They are assigned to the (001), (101) and (002) lines, respectively. Consequently, we can conclude that using more powerful laser intensity yields more crystallized films.

It is observed that intensity of the so-called xerogel peak at about 7.5° decreases gradually by increasing the intensity of the laser beam. Finally, the original structure of xerogel above 102 W/cm^2 ceases and polycrystalline V_2O_5 is created. Concerning the other peaks, they increase together with the intensity of the laser radiation.

The crystallite size D was calculated from the Scherrer equation using the XRD peak of the (001) reflection [14]. These calculations are shown in Table.1. The diameters of the V_2O_5 crystallites were calculated to be 44-81 nm in the lower intensity range. Using higher intensities structures become macrocrystalline. It must be noted that these size values correspond to a mean crystallite size on the spot where the X-ray passed through.

Name of the sample	Intensity (W/cm^2)	Mean crystallite size of V_2O_5 D (nm)
VO1	*Untreated sample*	
VO2	62	44.1
VO3	76	48.9
VO4	102	80.7
VO5	129	Macrocrystalline
VO6	169	Macrocrystalline

Table 1. Crystallite sizes in the function of laser intensity.

5.3.2. X-ray photoelectron spectroscopy

Fig.4. a. shows the spectra of the (a) untreated gel (VO1) and the (b) laser treated (VO5) sample with three intensive peaks corresponding to the core level orbitals of O (1s), V ($2p_{1/2}$) and V ($2p_{3/2}$), respectively. The signal of the O (1s) peak has a shoulder at the high binding energy (BE) side in both cases. In Fig.4. b. one can see the deconvolution, which reveals that the O (1s) spectrum area is the sum of 3 peaks. The one at 530.5 eV corresponds to the so-called "oxydic oxygen" and reflects the presence of vanadium oxide.

The peaks at 532.4 eV are due to the OH groups on the sample surface, while those at 533.5 eV are from C-O bonds and possibly water adsorbed on the surface. The typical spin-orbit splitting between V ($2p_{3/2}$) and V ($2p_{1/2}$) peaks is 7.2 eV. The BE positions of the V ($2p_{3/2}$) peak at 517.7 eV and the V ($2p_{1/2}$) peak at 524.9 eV are in good agreement with the previous works for orthorombic V_2O_5 films [15].

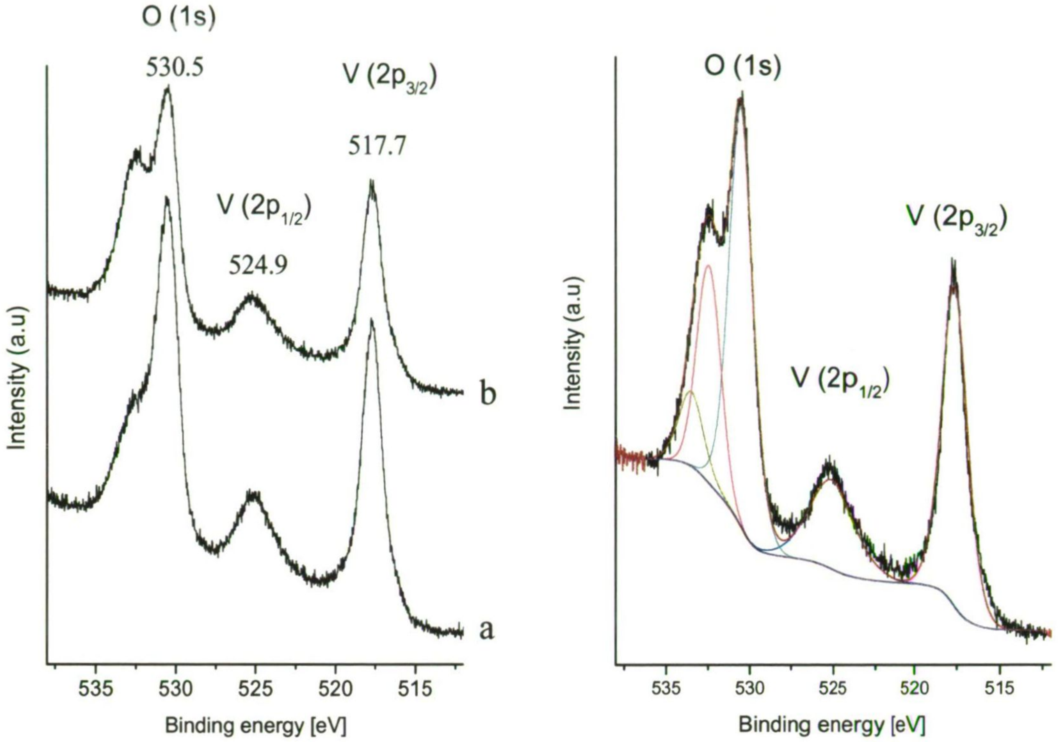

Fig.4.a. X-ray photoelectron spectra of the (a) untreated gel (VO1) and the (b) laser treated (VO5) sample. Fig.4.b. shows the deconvoluted X-ray photoelectron spectra of a sol-gel film (VO1).

The core level BE peaks, namely V (2p) and O (1s), are used to characterize the chemical state of vanadium in V_2O_5 films. There is a relationship between the core level BE and the charge state associated with an individual atom. An increase in the core level BE often indicates an increase in the positive charge of the atom [16]. The core level BE of V ($2p_{3/2}$) emission peak of metallic vanadium is at 512.4 eV [17]. For polycrystalline, stoichiometric V_2O_5, the V ($2p_{3/2}$) peak position is reported at 517.0 eV with a chemical shift of 4.6 eV characterizing the highest oxidation state of vanadium [18]. The FWHM of V ($2p_{1/2}$) is much broader than that of V ($2p_{3/2}$) due to the Coster-Kronig transitions [19].

Sample stoichiometry ratio $S_{i,j}$ is calculated from the XP spectra using the following formula [20]:

$$S_{i,j} = \frac{C_i}{C_j} = \frac{I_i / ASF_i}{I_j / ASF_j}$$

where C_i and C_j are the concentrations of the elements, I_i and I_j the background corrected intensities of the photoelectron emission lines and ASF_i and ASF_j the atomic sensitivity factors for photoionization of the i^{th} and j^{th} elements. For example the O to V ratio in stoichiometric V_2O_5 should be $S_{O,V} = 2.5$. This formula is only valid for homogenous element distributions in the sample. The O/V atom ratios were determined by deconvoluting the spectra of both the untreated and treated samples. The ratio was 1.8 for the untreated sample (VO1) and 2.3 for the treated one (VO5) showing the sub-stoichiometry of the films and the increment in O/V ratio due to laser radiation.

5.3.3. Morphology

5.3.3.1. Transmission electron microscopy

Collections of nanocrystals are observed in each sample. In Figs.5-6. untreated samples can be seen. Most of the nanocrystals are fibrillar-like particles with a length of about 150-200 nm and a width of about 10 nm.

In Figs.7-8. images after the laser treatment are seen (VO3). The originally fibrillar shaped particles are totally destroyed by the laser radiation and irregular shaped particles were obtained. Furthermore, Figs.7-8 justify the crystallite size calculations from the Sherrer equation.

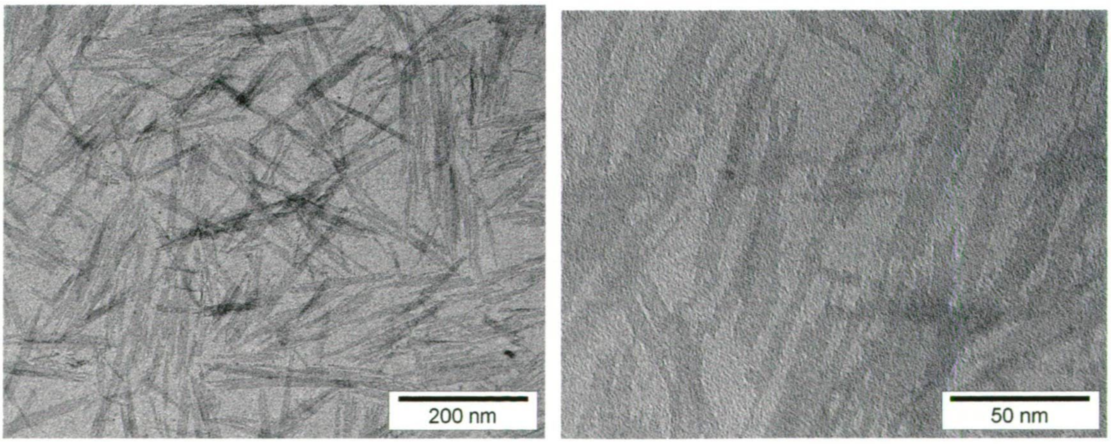

Figs.5-6. TEM images are seen before the laser treatment (VO1). Xerogel contains fibrillar-like particles with a length of about 150-200 nm and a width of about 10 nm.

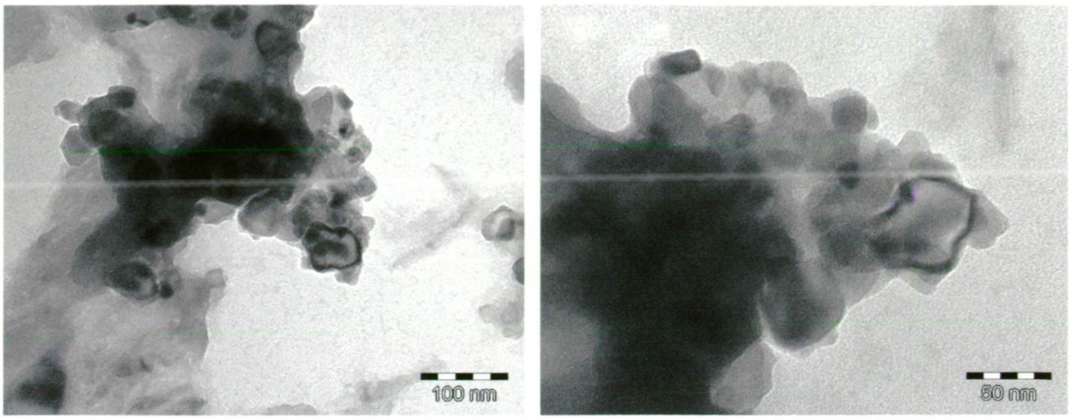

Figs.7-8. TEM images after the laser treatment are seen (VO3). Particles become irregular shaped due to laser irradiation in the range of about 40-80 nm diameters.

5.3.3.2. Scanning electron microscopy

In Figs.9-13. SEM images are seen. In Fig.9. one can see the difference between the laser treated (left hand side) and the untreated surface. In Figs.10.-11. higher magnification images are seen of the treated part where we can observe both the huge specific surface and the layered structure.

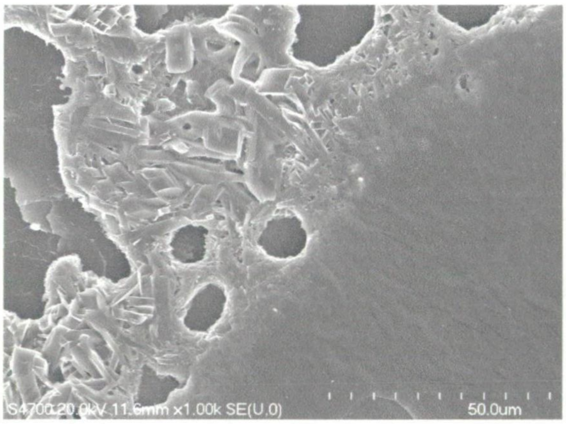

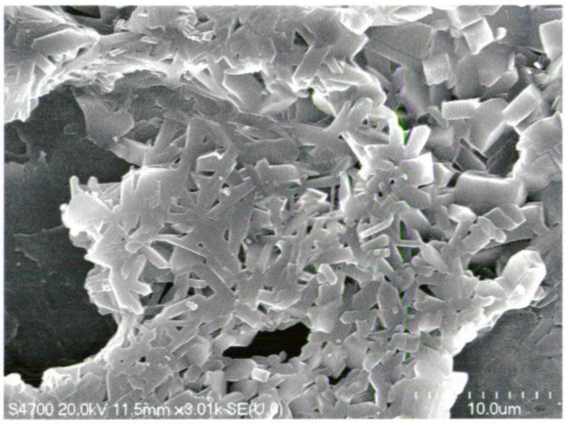

Fig.9. SEM image showing the irradiated and the untreated part of the sample (Intensity = 102 W/cm^2). Fig.10. SEM image showing the large specific surface caused by the laser radiation (Intensity = 102 W/cm^2).

This layered structure is shown also in Fig.12. with different magnifications. In the bottom-left part of the image, we can observe that layers are situated some tens of nanometers from each other.

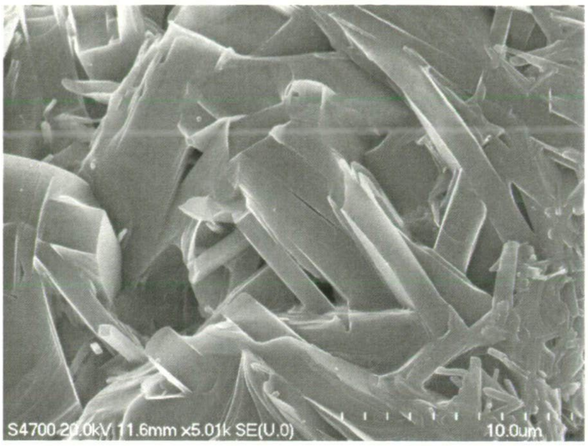

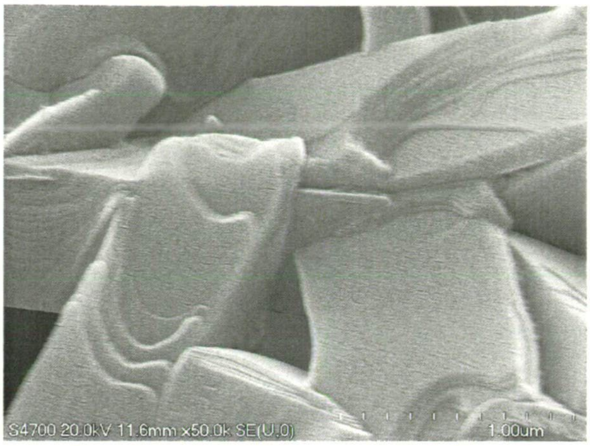

Fig.11. Higher magnification (5000 times) SEM image of the irradiated part showing the enlarged specific surface (Intensity = 102 W/cm^2). Fig.12. Layered structure can be observed in this high magnification (50000 times) SEM image of the irradiated part (Intensity = 102 W/cm^2).

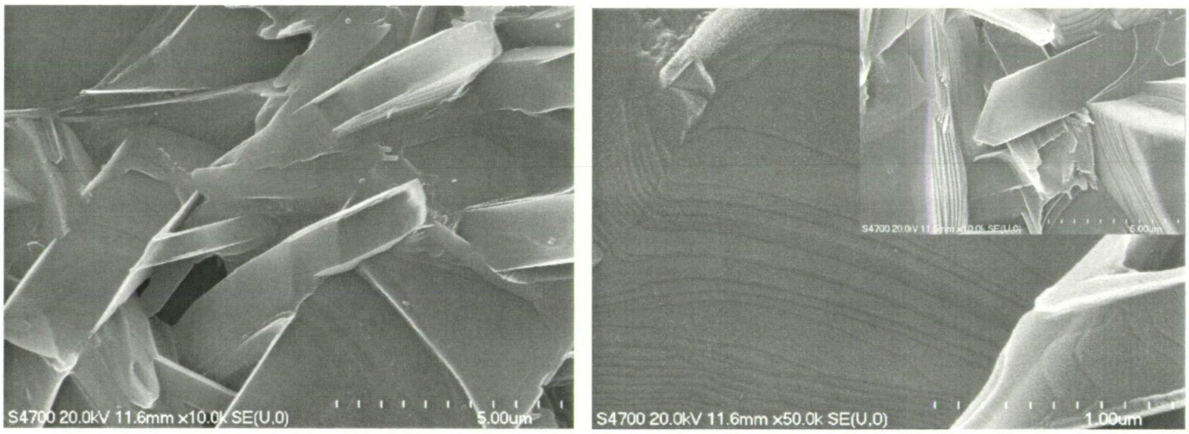

Fig.13. SEM image of the irradiated part. Layered structures are seen from two different views and magnifications. (Intensity is 102 W/cm^2.)

5.3. Conclusions of chapter 5.

We have synthesized V_2O_5 films by utilizing cw Nd:YAG laser radiation with varying the intensity of the laser radiation. XRD measurements show the peaks coincided with (001) reflections. The original structure of xerogel above 102 W/cm^2 ceases and polycrystalline V_2O_5 is created. At the same time, from TEM and SEM images we can conclude that the originally fibrillar-like particles were disappearing by the laser radiation. This can be related to the heating temperature by the laser radiation and can result in the release of water molecules, originally present in the particles.

XPS spectra after deconvolution proved the increment of the O/V ratio due to laser radiation.

At higher temperatures the oxygen flow into the sol-gel structure is enhanced therefore the oxygen diffusion becomes more intense yielding the creation of the most saturable oxide, the V_2O_5.

In the laser treated samples, irregular shaped and layer-structured V_2O_5 particles were obtained with apparently larger specific surface. Sol–gel procedure completed with laser treatment under well-defined experimental conditions was used to prepare V_2O_5.

References of chapter 5.

1. D. Wruck, S. Ramamurthi, M. Rubin, Thin Solid Films 182 (1989) 79.
2. J.B. Goodenough, Solid State Chem. 5 (1971) 45.
3. A. Suli, M. I. Torok, I. Hevesi, Thin Solid Films139 (1986) 233.
4. J.G. Zhang, J.M. McGraw, J.Turner, J. Electrochem. Soc. 144 (1997) 1630.
5. C. Julien, B. Yebka, J.P. Guesdon, Ionics 1 (1995) 316.
6. C. Julien E. Haro-Poniatowski, M.A. Camacho-Lopez, Mat. Sci. Eng B65 (1999)170-176
7. C.V. Ramana, O.M. Hussain, B. Srinivasulu Naidu, Thin Solid Films 305 (1997) 219-226
8. M. Ghanashyam Krishna, A.K. Bhattacharya, Mat. Sci. and Eng. B49 (1997) 166-171
9. W. Gulbinski, T. Suszko, D. Pailharey, Wear 254 (2003) 988–993
10. N.Özer, Thin Solid films 305 (1997) 80.
11. S.Beke, S. Giorgio, L. Kőrösi, submitted to Thin Solid Films (2006)
12. C.V. Ramana, R.J. Smith, O.M. Hussain, Phys. Stat. Sol. (a) 199, No.1, R4-R6 (2003)
13. D. Bauerle, Laser Processing and Chemistry, Springer, Heidelberg, 1996
14. Kaelbe, Handbook of X-rays, McGraw-Hill, New York, 1967
15. K. Wandelt, Surf. Sci. Rep. 2 (1982) 1.
16. A. Z. Moshfegh, A. Ignatiev, Thin Solid Films 198 (1991) 253.
17. R. Larsson, B. Folkesson, G. Schon, Chem. Scr. 3 (1973) 88.
18. R. J. Colton, A. M. Guzmann, J. W. Rabalais, J. Appl. Phys. 49 (1978) 409.
19. E. Antonides. E. C. Janse, G.A. Sawatzky, Phys.Rev.B 15 (1977) 4596.
20. C.D. Wagner, W.M. Riggs, L.E.Davis, J.F. Moulder, Handbook of X-ray Photoelectron Spectroscopy, Perkin Elmer Corporation, Eden Prairie, 1979

6. PERSPECTIVES AND APPLICATIONS

In chapter 3., we presented PLD for production of nanostructured vanadium oxides. Obviously, this method is also a great tool to ablate any kind of material including the ones in the biomedical field [1]. The coating of surfaces can play an important role inside biological structures (implants, othopedic screws, prosthesis). Coatings improve the biocompatibility of the surfaces, they can harden it or make it more resistant against mechanical stresses. Consequently, PLD can be a general methode in biomaterial synthesis as it makes possible to materials to be deposited on any kind of surface.

6.1. Utility of PS

Nanoporous silicon is a unique and versatile material that has several features that make it especially attractive for chemical and biological sensors, including a very high surface to volume ratio, simple and inexpensive fabrication techniques, and suitability for integration with silicon electronics. There are many potential device applications of PS such as electroluminescent devices, gas sensors, humidity sensors, waveguides and interference filters. The high surface area of PS and the perceived compatibility of the material with conventional Si microelectronics fabrication technologies has led to the proposal that it may be useful in sensor devices. The conductivity and capacitance of PS layers have been observed to change dramatically on adsorption of molecules to the PS surface.

As the application of this material is world-wide and enormous, this chapter can not deal with every aspect of it. Hereby, we would like to discuss briefly - through an example - an application concerning PS biosensing [2,3].

We know that biological and chemical sensors have an important and growing role in diverse fields including medical diagnosis, drug development, homeland security, and manufacturing. A PS based biosensor can be designed to measure small changes in the refractive index of PS that occur when exposed to chemical vapors or when biological molecules attach to the internal surfaces.

The concept of this kind of PS biosensor is that the internal surface of the porous silicon is coated with an interactant (e.g. biotin molecule) that selectively binds to a target substance (e.g. streptavidin protein) to be detected. When the target material is immobilized on the surface, the macroscopic optical properties of the porous silicon film change in a measurable way.

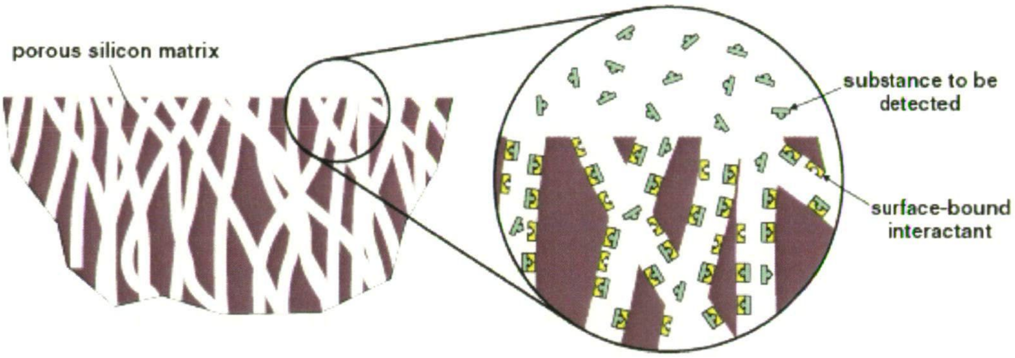

Fig.1. Concept of porous silicon biosensor from ref. [2].

This application is to present the utility of PS for optical sensing of biological and chemical substances that could provide unprecedented sensitivity in a device that can be readily fabricated with conventional silicon materials and techniques.

6. 2. Utility of vanadium oxides

Vanadium oxides like PS are very widely used materials in several fields of science. Hereby, we would like to show the perspectives of vanadium oxides focusing on the possible medical applications.

The general application aspect of vanadium oxides relies on its catalytic properties. As catalysis is more effective in case of enlarged surfaces, therefore nanostructural catalytic materials are much more useful than the bulk ones.

Another application area of vanadium oxides is the implantable medical devices like pacemakers. Today's pacemakers typically use lithium iodine batteries and defibrillators employ lithium silver vanadium oxide [4]. The realization of long life batteries is the condition of using fully implantable hearing devices and cochlear implants [5,6.]. Any increase in the service life of implantable medical devices is highly desirable and important. It would be essential to use power sources with higher energy densities and lower internal resistance and also to reduce the size of devices.

References of chapter 6.:

1. R. Major, J. Bonarski, J. Morgiel, B. Major, E. Czarnowska, R. Kustosz, J.M. Lackner and W. Waldhauser, Surface and Coatings Technology, Volume 200, Issues 22-23, 20 June 2006, 6340-6345

2. A. M. Rossi, L. Wang, V. Reipa and T. E. Murphy, "Porous Silicon Biosensor for MS2 Virus", to appear in Biosensors and Bioelectronics. (2007).

3. Victor S.-Y. Lin, Kianoush Motesharei, Keiki-Pua S. Dancil, Michael J. Sailor, M. Reza Ghadiri, Science Vol. 278. no. 5339, 840 – 843. 1997

4. Venkateswara Sarma Mallela, V. Ilankumaran, N. Srinivasa Rao, Indian Pacing Electrophysiol J. 2004 October–December; 4(4): 201–212.

5. Cohen N., The totally implantable cochlear implant. Ear Hear. 2007 Apr 28 (2 Suppl.): 100-101.

6. Backous D.D., Duke W., Implantable middle ear hearing devices: current state of technology and market challenges. Curr. Opin. Otolaryngol. Head Neck Surg. 2006 Oct.14(5):314-8.

ORIGINAL PAPERS: